Operating conditions and thermodynamic bounds of dual radiative heat engines

Julien Legendre and Pierre-Olivier Chapuis
Univ Lyon, CNRS, INSA-Lyon, Université Claude Bernard Lyon 1, CETHIL UMR5008, F-69621, Villeurbanne, France
(Dated: February 13, 2024)

A dual radiative heat engine is a device made of two facing optoelectronic components (diodes) and capable of generating electrical power from heat. It can operate in three different regimes depending on the component biases, namely in thermoradiative-negative electroluminescent (TRNEL), thermoradiative-photovoltaic (TRPV) or thermophotonic (TPX) regimes. The use of dual engines gives access to operating conditions which are unachievable by single radiative engines such as thermophotovoltaic systems: at the radiative limit, TRNEL devices systematically reach the Carnot efficiency, while TPX devices can achieve large power outputs by means of electroluminescent enhancement. Upper bounds of the maximum power output and related efficiency achieved by dual engines are derived analytically, and compared to usual bounds. Spectral filtering and nonradiative recombinations are also briefly considered. This work provides common framework and guidelines for the study of radiative engines, which represent a promising solution for reliable and scalable energy conversion.

The conversion of heat into electrical power by optoelectronic means has gathered sizeable attention in the past decades. The two most popular solutions are photovoltaics (PV) for solar application, and thermophotovoltaics (TPV) [1–4]. In the latter case, the radiation comes from a hot emitter maintained at a high temperature by the input heat. This gives access to a broad range of applications, for instance in latent heat TPV batteries [5]. Apart from PV and TPV, other optoelectronic systems are able to convert heat to electricity. One is the thermoradiative (TR) cell: as opposed to the PV cell, it is able to generate electrical power by emitting negative electroluminescent radiation to the cold surroundings [6, 7] (e.g. the night sky, outer space) or towards a cold absorber [8]. TR cells, along with PV and TPV cells, are single radiative heat engines: they are heat engines in which one active component produces electrical power either by emitting or absorbing radiation [9]. Their typical electrical characteristic is provided in Section I of Supp. Mat. [10]. Radiative engines are part of the larger group of solid-state heat engines [11], along with thermoelectric [12] and thermionic generators [13], and thus compete with such systems in the field of reliable and scalable energy conversion.

It is also possible to couple two different optoelectronic components into a dual radiative heat engine (see Fig. 1). One such dual engine is the thermoradiative-photovoltaic (TRPV) device [14, 15], in which a hot TR cell is coupled to a cold PV cell: both components are then able to generate electrical power, although production by the TR cell limits its emission due to negative electroluminescence, and therefore reduces the PV cell production. Nonetheless, having two components provides better control of the operating conditions. Thermophotonics (TPX) [16–18] has also gathered interest recently. In such a device, the hot emitter is a light-emitting diode (LED). While an LED consumes electrical power, it is able to emit electroluminescent radiation towards the PV cell with an above-unity wall-plug efficiency, enabling a significant increase in power output. Recently, TPX devices have mostly been studied in near-field operation, as near-field radiation further increases the power output [19, 20] and limits the impact of non-radiative losses [21].

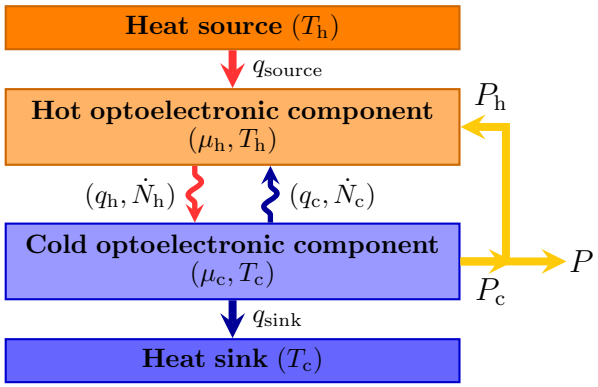

FIG. 1: Representation of the dual radiative engine (here in a thermophotonic configuration).

Although the aforementioned systems are all radiative heat engines and share the same core physical laws, they are studied independently of one another in the literature. This makes the comparison of their performance less straightforward. Therefore, in the current Letter, we provide a complete overview of the performance of dual radiative heat engines achieved for various bandgaps, and highlight the interests of each operating regime. In particular, we focus on the maximum achievable power and efficiency, and derive analytical upper bounds for these two quantities.

In the following, we assume that the dual engine operates in the far field. To maximise the achievable power output, the emission of radiation is assumed to follow the

modified Planck law. Furthermore, the bandgaps of the two components are assumed to be equal, and the radiation exchanged below the bandgap is neglected to obtain an upper bound of the efficiency. Thus, the emitted photon flux density $\dot{N}$ and the related heat flux density q can be expressed as

$$\dot{N}_i = \frac{1}{4\pi^2 c^2 \hbar^3} \int_{E_g}^{\infty} \frac{E^2}{\exp\left(\frac{E-\mu_i}{k_B T_i}\right) - 1} dE, \tag{1a}$$

$$q_i = \frac{1}{4\pi^2 c^2 \hbar^3} \int_{E_g}^{\infty} \frac{E^3}{\exp\left(\frac{E-\mu_i}{k_B T_i}\right) - 1} dE, \tag{1b}$$

where i relates to the emitting body (either "h" or "c") with bandgap energy E_g and temperature T_i. μ_i is the chemical potential of the emitted radiation, which must remain strictly smaller than E_g and is assumed to be related to the voltage U_i applied to the component through $\mu_i = eU_i$ [22, 23], e being the elementary charge. The above integrals can be expressed analytically using polylogarithms [24], leading to

$$\dot{N}_i = \frac{(k_B T_i)^3}{4\pi^2 c^2 \hbar^3} \big(e_{g,i}^2 \,\mathrm{Li}_1(e^{-x_i}) + 2e_{g,i}\,\mathrm{Li}_2(e^{-x_i}) + 2\,\mathrm{Li}_3(e^{-x_i})\big), \tag{2a}$$

$$q_i = \frac{(k_B T_i)^4}{4\pi^2 c^2 \hbar^3} \big(e_{g,i}^3 \,\mathrm{Li}_1(e^{-x_i}) + 3e_{g,i}^2\,\mathrm{Li}_2(e^{-x_i}) + 6e_{g,i}\,\mathrm{Li}_3(e^{-x_i}) + 6\,\mathrm{Li}_4(e^{-x_i})\big), \tag{2b}$$

where Li_n is the n-th order polylogarithm, $e_{g,i} = E_g/k_B T_i$ and $x_i = (E_g - \mu_i)/k_B T_i$. Finally, to obtain an upper bound of the dual engine performance, we assume that any active component operates at the radiative limit (i.e. without any non-radiative losses). The electrical power generated by a component i facing a component j is then

$$P_i = U_i \cdot e(\dot{N}_j - \dot{N}_i) = \mu_i(\dot{N}_j - \dot{N}_i). \tag{3}$$

The total power output is therefore

$$P = (\mu_c - \mu_h)(\dot{N}_h - \dot{N}_c). \tag{4}$$

Since $q_{source} = q_h - q_c + P_h$, the overall heat engine efficiency is

$$\eta = \frac{P}{q_{source}} = \frac{(\mu_c - \mu_h)(\dot{N}_h - \dot{N}_c)}{q_h - q_c - \mu_h(\dot{N}_h - \dot{N}_c)}. \tag{5}$$

Using these constitutive equations, we start by studying how the power output of the dual engine varies in the (μ_h,μ_c) plane. The results obtained considering $T_h = 600$ K and $E_g = 5k_B T_h$ are illustrated in Fig. 2a. The dual system can also operate as a heat pump [25, 26], and we indicate in a blue colour scale the cooling power. Note that such high cooling powers can only be achieved because below-bandgap radiation is neglected [27].

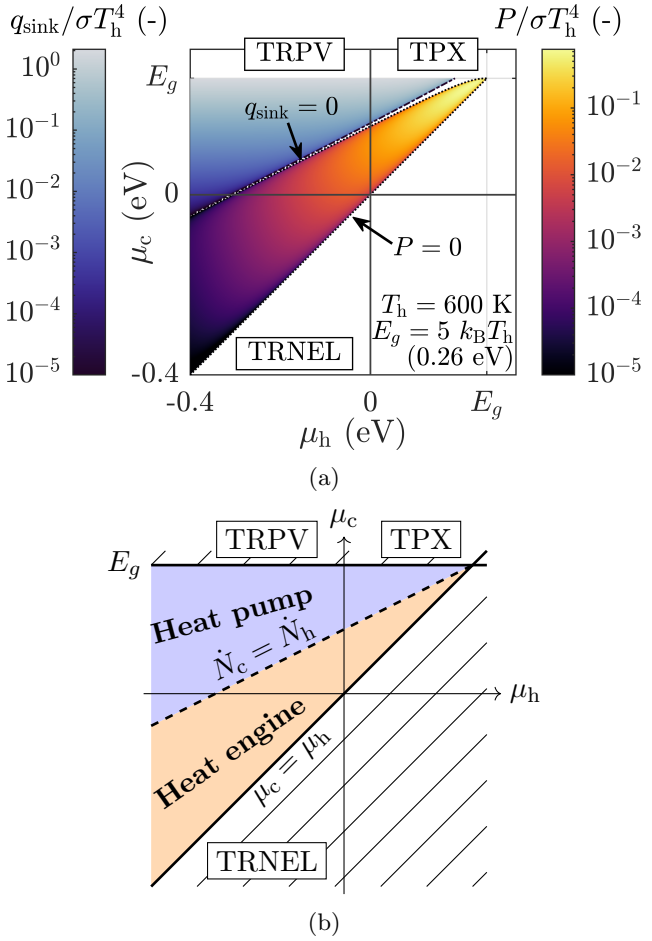

FIG. 2: (a) Performance of dual radiative systems operating as heat engines or heat pumps, at the radiative limit and for $E_g = 5k_B T_h = 0.26$ eV. (b) Operating regions of dual radiative systems in the limit of an infinite bandgap.

For the bandgap selected, the dual system is able to operate both as a heat engine and a heat pump in three of the four quadrants: namely, the TPX quadrant (upper-right), the TRPV quadrant (upper-left) but also the "TRNEL" quadrant, in which a cold negative electroluminescent (NEL) diode consumes electrical power to limit the radiation sent to the hot facing TR cell. To the best of our knowledge, the TRNEL device has never been mentioned in literature. Globally, both the power output and the cooling power increases with μ_c, while P also increases with μ_h: the maximum power point (MPP) is therefore located in the TPX quadrant, while the maximum cooling power is reached in TRPV operation for $\mu_c \to E_g$. Despite $\mu_c \to E_g$, the cooling power converges towards a constant value, as demonstrated in [28]. Additionally, note that for low E_g, the TPX device becomes unable to perform cooling (see Section II of Supp. Mat. [10]).

Note how the dual system does not switch directly from

heat engine to heat pump operation as μ varies. Indeed, there is a narrow region in-between where the system is neither able to generate electrical power nor to cool the cold source. This gap can especially be observed when $E_g - \mu_h$ becomes lower than $k_\mathrm{B}T_\mathrm{h}$, but globally narrows down as the bandgap increases: in the limit of infinite bandgaps, the two operating regions become adjacent as $q_\mathrm{h} = q_\mathrm{c}$ and $\dot{N}_\mathrm{h} = \dot{N}_\mathrm{c}$ are equivalent. This is schematised in Fig. 2b. In this situation, the term related to the lowest-order polylogarithm dominates in the expressions provided in Eq. (2). By linearising Li_1, we obtain that the transition from one region to the other - which corresponds to open-circuit conditions - occurs approximately for

$$\mu_\mathrm{c} = \frac{T_\mathrm{c}}{T_\mathrm{h}}\mu_\mathrm{h} + \left(1 - \frac{T_\mathrm{c}}{T_\mathrm{h}}\right) E_g + k_\mathrm{B}T_\mathrm{c} \ln\left(\frac{T_\mathrm{h}}{T_\mathrm{c}}\right), \qquad (6)$$

this linearised expression being a very good approximation as long as $E_g - \mu_i \gg k_\mathrm{B}T_i$. The other side of the power production region is simply delimited by the condition $\mu_\mathrm{h} = \mu_\mathrm{c}$. These two expressions have already been mentioned for TPX devices in [20].

To quantify and compare the performance of TPX, TRPV and TRNEL devices, we provide in Fig. 3 the $\eta - P$ plots obtained by varying both μ_h and μ_c, considering three different bandgaps and a heat source temperature of 600 K. For each device, the shaded area corresponds to achievable operation, while the full line is the envelope of this area. Looking at the three cases considered, it is first interesting to notice that while the shape of the admissible $\eta - P$ area changes significantly when considering each engine individually, it remains mostly unchanged with varying bandgaps for the full dual radiative engine. For any of the bandgaps considered, the efficiency at maximum power remains mostly constant (between 28% and 34% of the Carnot efficiency $\eta_\mathrm{C} = 1 - T_\mathrm{c}/T_\mathrm{h}$), while the maximum efficiency is always η_C and is reached at zero power.

If we now compare the different engines, TRNEL appears to be the optimal choice to maximise the efficiency, being always able to reach the Carnot efficiency. Note that this is true only because it operates at the radiative limit: in Section III of Supp. Mat. [10], we analyse the impact of non-radiative losses on performance by considering a spectrally flat quantum efficiency, and pinpoint that the interest of TRNEL operation vanishes when the quantum efficiency goes significantly below unity. Even at the radiative limit, the advantage of TRNEL operation shrinks for large bandgap: as $E_g \to \infty$, all radiative engines are able to approach the Carnot efficiency in open-circuit conditions. This has already been demonstrated for TR [6, 7] and TPV [29], but can in fact be shown for any radiative engine. In the limit of an infinite bandgap $(q_\mathrm{h} - q_\mathrm{c})/(\dot{N}_\mathrm{h} - \dot{N}_\mathrm{c}) \to E_g$, leading η to be expressed as $(\mu_\mathrm{c} - \mu_\mathrm{h})/(E_g - \mu_\mathrm{h})$. Using Eq. (6), and keeping in mind that $E_g - \mu_\mathrm{h} \gg k_\mathrm{B}T_\mathrm{h}$, we obtain that the efficiency in

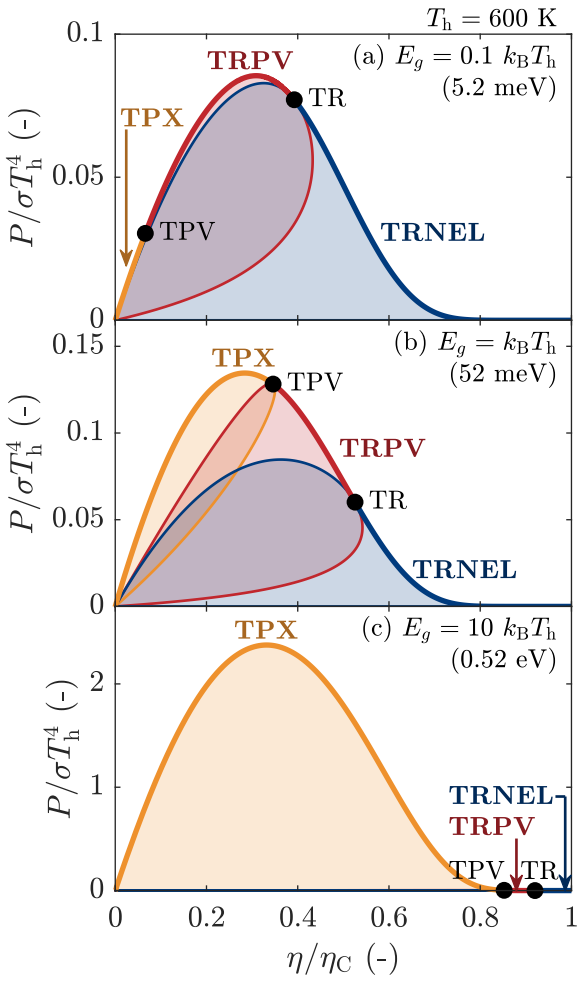

FIG. 3: $\eta - P$ plots of dual radiative engines at the radiative limit, for $T_\mathrm{h} = 600$ K and for various bandgaps.

open-circuit conditions equals η_C.

In contrast, to maximise the power output, TPX is almost always the best candidate, TRPV becoming optimal only for very low bandgap energies (here, for $E_g < k_\mathrm{B}T_\mathrm{h} \approx 0.05$ eV) which are not achievable physically. This remains true for lower or higher heat source temperatures (see Section IV of Supp. Mat. [10]). TPX devices generally outperform other radiative engines in terms of power output because the hot emitter operates as an LED: it is therefore able to largely enhance its emission by electroluminescence, increasing consequently the various energy flows in the system. For high enough bandgaps, this can even cause P_max to exceed σT_h^4 (see Fig. 3c), which is physically impossible for single radiative engines.

While TRNEL devices allow maximising efficiency and TPX devices power, TRPV systems can in some conditions provide interesting trade-offs between power and efficiency (see Fig. 3b). However, this can only be observed for low bandgaps (a few $k_\mathrm{B}T_\mathrm{h}$ at most) which are

hardly achievable for the heat source temperature considered.

The study of $\eta - P$ plots directly highlights that the maximum efficiency of dual radiative engines is always the Carnot efficiency, reached for zero power output. Regarding the MPP, it was observed that $P_{\max}$ increases significantly with E_g while η_{MPP} varies only slowly, but no analytical expressions of these quantities have yet been formulated. Therefore, in the following, we focus on the analytical derivation of $P_{\max}$ and η_{MPP}. To do so, we consider once again that $E_g \to \infty$, since this allows reaching the largest possible power output (see Section V of Supp. Mat. [10]). By doing so, the Li_1 term dominates the expressions provided in Eq. (2). Using that $\mu_{\mathrm{c}} - \mu_{\mathrm{h}} = x_{\mathrm{h}} k_{\mathrm{B}} T_{\mathrm{h}} - x_{\mathrm{c}} k_{\mathrm{B}} T_{\mathrm{c}}$, and defining X_i as $\exp(-x_i)$, the power output can be expressed as:

$$P = \frac{E_g^2 k_{\mathrm{B}}^2 T_{\mathrm{h}}^2}{4\pi^2 c^2 \hbar^3} \left(\ln(X_{\mathrm{h}}) - \frac{T_{\mathrm{c}}}{T_{\mathrm{h}}} \ln(X_{\mathrm{c}}) \right) \times \left(\ln(1 - X_{\mathrm{h}}) - \frac{T_{\mathrm{c}}}{T_{\mathrm{h}}} \ln(1 - X_{\mathrm{c}}) \right), \tag{7}$$

since $\mathrm{Li}_1(x) = \ln(1-x)$. By using the symmetry of this expression with respect to X_{h} and X_{c}, one can show that P reaches its maximum for $X_{\mathrm{h}} = X_{\mathrm{c}} = 1/2$, thus for $\mu_i = E_g - \ln(2) k_{\mathrm{B}} T_i$ (see Section VI of Supp. Mat. [10]). Consequently, the maximum power output is

$$P_{\max} = \frac{1}{\hbar} \left(\frac{\ln(2) E_g k_{\mathrm{B}} (T_{\mathrm{h}} - T_{\mathrm{c}})}{2\pi c \hbar} \right)^2, \tag{8}$$

and varies quadratically with both the bandgap energy and the temperature difference. Such variations were already pointed out in [28], although without a complete closed-form expression. Since $E_g \gg k_{\mathrm{B}} T_i$, both chemical potentials are greater than 0 and the maximum is reached in TPX regime, consistently with the results from Fig. 3.

To derive a closed-form expression of the efficiency at maximum power, we use that $x_{\mathrm{h,MPP}} = x_{\mathrm{c,MPP}} = \ln(2)$ to obtain $(\mu_{\mathrm{c,MPP}} - \mu_{\mathrm{h,MPP}})/(E_g - \mu_{\mathrm{h,MPP}}) = \eta_{\mathrm{C}}$. Dividing both the numerator and the denominator of Eq. (5) by $(\dot{N}_{\mathrm{h}} - \dot{N}_{\mathrm{c}})(E_g - \mu_{\mathrm{h}})$, one gets

$$\eta_{\mathrm{MPP}} = \frac{\eta_{\mathrm{C}}}{1 + \left(\frac{1}{\rho} - 1 \right) \frac{1}{\ln(2)} \frac{E_g}{k_{\mathrm{B}} T_{\mathrm{h}}}}, \tag{9}$$

where $\rho = E_g(\dot{N}_{\mathrm{h}} - \dot{N}_{\mathrm{c}})/(q_{\mathrm{h}} - q_{\mathrm{c}})$ corresponds to the fraction of radiative energy being useful to optoelectronic conversion. To express it, both Li_1 and Li_2 terms are necessary. One obtains

$$\left(\frac{1}{\rho} - 1 \right) \frac{1}{\ln(2)} \frac{E_g}{k_{\mathrm{B}} T_{\mathrm{h}}} \underset{E_g \to \infty}{\sim} (2 - \eta_{\mathrm{C}}) \frac{1}{\ln(2)} \frac{\mathrm{Li}_2(1/2)}{\mathrm{Li}_1(1/2)}. \tag{10}$$

The polylogarithmic terms having closed-form expressions for $x = 1/2$, the efficiency at maximum power obtained as $E_g \to \infty$ is

$$\eta_{\mathrm{MPP},E_g \to \infty} = \frac{\eta_{\mathrm{C}}}{1 + (2 - \eta_{\mathrm{C}})\chi}, \tag{11}$$

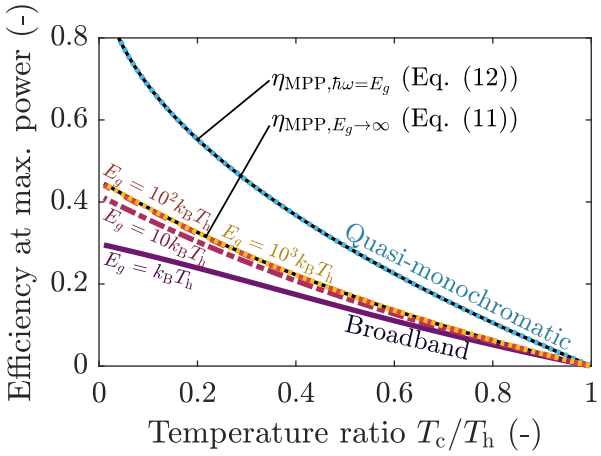

FIG. 4: Variation of the efficiency at maximum power with the heat source temperature. For simplicity, only the TPX quadrant has been considered.

χ being a constant equal to $\frac{1}{2}\left(\frac{1}{6}\left(\frac{\pi}{\ln(2)}\right)^2 - 1\right) \approx 1.21$. The temperature variation of $\eta_{\mathrm{MPP},E_g\to\infty}$ is provided in Fig. 4 (black line), and matches well the numerical results obtained for bandgaps larger than $100 k_{\mathrm{B}} T_{\mathrm{h}}$. It also gives a good estimate of the efficiency obtained for standard bandgaps, as long as $E_g \gg k_{\mathrm{B}} T_{\mathrm{h}}$: for $T_{\mathrm{h}} = 600$ K, $\eta_{\mathrm{MPP},E_g\to\infty} = 17.7\%$ while $\eta_{\mathrm{MPP,1\ eV}} = 17.1\%$ and $\eta_{\mathrm{MPP,0.52\ eV}} = 16.6\%$.

To better understand how efficient dual radiative engines are at maximum power, one can compare Eq. (11) with classical upper bounds for η_{MPP}. We choose to perform the comparison with the Novikov-Curzon-Ahlborn [30, 31] efficiency $\eta_{\mathrm{NCA}} = 1 - \sqrt{T_{\mathrm{c}}/T_{\mathrm{h}}}$ and the Schmiedl-Seifert [32] efficiency $\eta_{\mathrm{SS}} = 2\eta_{\mathrm{C}}/(4 - \eta_{\mathrm{C}})$, which were found to be efficiency bounds for endoreversible and exoreversible thermoelectric generators respectively [33]. For the temperatures previously considered, both efficiencies are close to 29%, hence 11 percent points higher than $\eta_{\mathrm{MPP},E_g\to\infty}$. This significant difference, which highlights the presence of additional losses in radiative engines, can be attributed to thermalisation losses - i.e., to the fraction of radiative energy exchanged which is useless to optoelectronic conversion. To prove this, we now consider that the radiation is quasi-monochromatic around E_g, which makes the ratio ρ equal to 1. In this scenario, $\mu_{i,\mathrm{MPP}}$ is found to tend towards E_g (see Section VII of Supp. Mat. [10]). Then, the Bose-Einstein distributions can be simplified using that $[\exp(x) - 1]^{-1} \sim x^{-1}$ around 0. Setting any of the two partial derivatives of P with respect to μ_i to zero leads to

$$\eta_{\mathrm{MPP},\hbar\omega=E_g} = 1 - \sqrt{\frac{T_{\mathrm{c}}}{T_{\mathrm{h}}}}, \tag{12}$$

exactly the Novikov-Curzon-Ahlborn efficiency. δE being the radiation spectral bandwidth, the maximum power

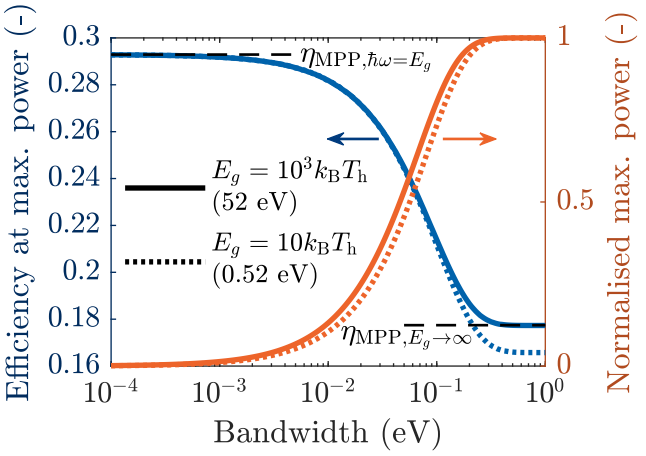

FIG. 5: Variation of the maximum power and related efficiency for varying spectral bandwidth, considering $T_\mathrm{h} = 600$ K. For simplicity, only the TPX quadrant has been considered.

output is then

$$P_\mathrm{max} = \frac{1}{\hbar}\left(\frac{E_g\sqrt{k_\mathrm{B}}(\sqrt{T_\mathrm{h}}-\sqrt{T_\mathrm{c}})}{2\pi c\hbar}\right)^2 \delta E, \qquad (13)$$

an expression similar to Eq. (8). Since P goes to zero as $\delta E \to 0$, there is a trade-off between power and efficiency as the bandwidth varies, as illustrated in Fig. 5: to achieve non-zero output power, the efficiency must fall below the usual bounds. It is noteworthy that the efficiency starts to decrease for bandwidths as low as few meV (corresponding to a quality factor $Q = E_g/\delta E$ close to 100 for $E_g = 0.52$ eV), while reaching the broadband limit for a bandwidth of few tenths of eV (i.e. for $Q \approx 1$ considering $E_g = 0.52$ eV). If the efficiency at maximum power is too low for a given application, two main leverages are thus available to increase it, although at the expense of power: decrease the radiation bandwidth, or change μ_h and μ_c to move in the broadband $\eta - P$ plots provided in Fig. 3, which can allow exceeding the aforementioned bounds [4]. The interest of each of these leverages depends on the bandgap, and on how far the system operates from the radiative limit. In some cases, spectral filtering can allow extending the region of achievable operating conditions, limiting the power loss undergone when high efficiency is required (see Section VIII of Supp. Mat [10]).

In conclusion, we have studied the power output and efficiency achievable by dual radiative heat engines, especially when they operate at the radiative limit. A unified view allows shining light on their similarities and respective merits. In particular, TRNEL devices are found to systematically reach Carnot efficiency, while TPX devices are almost always the best dual engines in terms of power output, and offer the broadest range of operating conditions of all dual engines for bandgaps over a few $k_\mathrm{B}T_\mathrm{h}$. We have analytically derived an upper bound for the maximum power and related efficiency, the latter mostly lying between 30% and 40% of η_C and being several percent points below usual efficiency bounds due to thermalisation losses (11 points below for $T_\mathrm{h} = 600$ K). Interestingly, spectral filtering can mitigate part of the power loss when high efficiencies are targeted. In practice, below-bandgap radiation, more rigorous non-radiative losses and resistive losses shall be included, as well as thermal resistance effects at the thermostats which reduce the operating temperature difference $T_\mathrm{h} - T_\mathrm{c}$ [23]. In addition, it would be worth investigating how the performance of such engines changes in the near field, where radiative emission exceeds the modified Planck law [19, 20, 23].

This work has received funding from the European Union's Horizon 2020 research and innovation programme under Grant Agreement No. 951976 (TPX-Power project). The authors thank T. Châtelet, P. Kivisaari, O. Merchiers, J. Oksanen and J. van Gastel.

[1] T. Burger, C. Sempere, B. Roy-Layinde, and A. Lenert, Present Efficiencies and Future Opportunities in Thermophotovoltaics, Joule **4**, 1660 (2020).
[2] A. LaPotin, K. L. Schulte, M. A. Steiner, K. Buznitsky, C. C. Kelsall, D. J. Friedman, E. J. Tervo, R. M. France, M. R. Young, A. Rohskopf, S. Verma, E. N. Wang, and A. Henry, Thermophotovoltaic efficiency of 40%, Nature **604**, 287 (2022).
[3] E. J. Tervo, R. M. France, D. J. Friedman, M. K. Arulanandam, R. R. King, T. C. Narayan, C. Luciano, D. P. Nizamian, B. A. Johnson, A. R. Young, L. Y. Kuritzky, E. E. Perl, M. Limpinsel, B. M. Kayes, A. J. Ponec, D. M. Bierman, J. A. Briggs, and M. A. Steiner, Efficient and scalable GaInAs thermophotovoltaic devices, Joule **6**, 2566 (2022).
[4] M. Giteau, M. F. Picardi, and G. T. Papadakis, Thermodynamic performance bounds for radiative heat engines, Physical Review Applied **20**, L061003 (2023).
[5] A. Datas, A. López-Ceballos, E. López, A. Ramos, and C. del Cañizo, Latent heat thermophotovoltaic batteries, Joule **6**, 418 (2022).
[6] R. Strandberg, Theoretical efficiency limits for thermoradiative energy conversion, Journal of Applied Physics **117**, 055105 (2015).
[7] A. Pusch, J. M. Gordon, A. Mellor, J. J. Krich, and N. J. Ekins-Daukes, Fundamental Efficiency Bounds for the Conversion of a Radiative Heat Engine's Own Emission into Work, Physical Review Applied **12**, 064018 (2019).
[8] P. Santhanam and S. Fan, Thermal-to-electrical energy conversion by diodes under negative illumination, Physical Review B **93**, 161410 (2016).
[9] E. J. Tervo, E. Bagherisereshki, and Z. M. Zhang, Near-field radiative thermoelectric energy converters: a review, Frontiers in Energy **12**, 5 (2018).
[10] See Supplemental Material for more details on the electrical characteristic of optoelectronic components, on the analytical developments, and on the impact of

bandgap, heat source temperature, non-radiative losses and bandgap filtering on dual engines' performance.

[11] C. Melnick and M. Kaviany, From thermoelectricity to phonoelectricity, Applied Physics Reviews **6**, 021305 (2019).

[12] X.-L. Shi, J. Zou, and Z.-G. Chen, Advanced Thermoelectric Design: From Materials and Structures to Devices, Chemical Reviews **120**, 7399 (2020).

[13] K. A. Abdul Khalid, T. J. Leong, and K. Mohamed, Review on Thermionic Energy Converters, IEEE Transactions on Electron Devices **63**, 2231 (2016).

[14] T. Liao, Z. Yang, X. Chen, and J. Chen, Thermoradiative–Photovoltaic Cells, IEEE Transactions on Electron Devices **66**, 1386 (2019).

[15] E. J. Tervo, W. A. Callahan, E. S. Toberer, M. A. Steiner, and A. J. Ferguson, Solar Thermoradiative-Photovoltaic Energy Conversion, Cell Reports Physical Science **1**, 100258 (2020).

[16] N.-P. Harder and M. A. Green, Thermophotonics, Semiconductor Science and Technology **18**, S270 (2003).

[17] S. McSherry, T. Burger, and A. Lenert, Effects of narrowband transport on near-field and far-field thermophotonic conversion, Journal of Photonics for Energy **9**, 032714 (2019).

[18] T. Sadi, I. Radevici, B. Behaghel, and J. Oksanen, Prospects and requirements for thermophotonic waste heat energy harvesting, Solar Energy Materials and Solar Cells **239**, 111635 (2022).

[19] B. Zhao, K. Chen, S. Buddhiraju, G. R. Bhatt, M. Lipson, and S. Fan, High-performance near-field thermophotovoltaics for waste heat recovery, Nano Energy **41**, 344 (2017).

[20] J. Legendre and P.-O. Chapuis, GaAs-based near-field thermophotonic devices: Approaching the idealized case with one-dimensional PN junctions, Solar Energy Materials and Solar Cells **238**, 111594 (2022).

[21] J. Legendre and P.-O. Chapuis, Overcoming non-radiative losses with AlGaAs PIN junctions for near-field thermophotonic energy harvesting, Applied Physics Letters **121**, 193902 (2022).

[22] W. A. Callahan, D. Feng, Z. M. Zhang, E. S. Toberer, A. J. Ferguson, and E. J. Tervo, Coupled Charge and Radiation Transport Processes in Thermophotovoltaic and Thermoradiative Cells, Physical Review Applied **15**, 054035 (2021).

[23] J. Legendre, *Theoretical and numerical analysis of near-field thermophotonic energy harvesters*, Ph.D. thesis, INSA Lyon, available at `https://theses.fr/2023ISAL0094` (2023).

[24] M. A. Green, Analytical treatment of Trivich-Flinn and Shockley-Queisser photovoltaic efficiency limits using polylogarithms, Progress in Photovoltaics: Research and Applications **20**, 127 (2012).

[25] P. Santhanam, D. J. Gray, and R. J. Ram, Thermoelectrically Pumped Light-Emitting Diodes Operating above Unity Efficiency, Physical Review Letters **108**, 097403 (2012).

[26] I. Radevici, J. Tiira, T. Sadi, S. Ranta, A. Tukiainen, M. Guina, and J. Oksanen, Thermophotonic cooling in GaAs based light emitters, Applied Physics Letters **114**, 051101 (2019).

[27] T. Châtelet, J. Legendre, O. Merchiers, and P.-O. Chapuis, Performances of far and near-field thermophotonic refrigeration in the detailed-balance approach, submitted (2024).

[28] B. Zhao and S. Fan, Chemical potential of photons and its implications for controlling radiative heat transfer, in *Annual Review of Heat Transfer*, Vol. 23 (2020) Chap. 10, pp. 397–431.

[29] B. Roux, C. Lucchesi, J.-P. Perez, P.-O. Chapuis, and R. Vaillon, Main performance metrics of thermophotovoltaic devices: analyzing the state of the art, Journal of Photonics for Energy, accepted and in press (2024).

[30] I. I. Novikov, Efficiency of an atomic power generating installation, The Soviet Journal of Atomic Energy **3**, 1269 (1957).

[31] F. L. Curzon and B. Ahlborn, Efficiency of a Carnot engine at maximum power output, American Journal of Physics **43**, 22 (1975).

[32] T. Schmiedl and U. Seifert, Efficiency at maximum power: An analytically solvable model for stochastic heat engines, Europhysics Letters **81**, 20003 (2008).

[33] Y. Apertet, H. Ouerdane, C. Goupil, and P. Lecoeur, Irreversibilities and efficiency at maximum power of heat engines: The illustrative case of a thermoelectric generator, Physical Review E **85**, 031116 (2012).

Supplemental material
Operating conditions and thermodynamic bounds of dual radiative heat engines

Julien Legendre and Pierre-Olivier Chapuis
Univ Lyon, CNRS, INSA-Lyon, Université Claude Bernard Lyon 1, CETHIL UMR5008, F-69621, Villeurbanne, France
(Dated: February 13, 2024)

I. ELECTRICAL CHARACTERISTIC OF OPTOELECTRONIC COMPONENTS

We provide in Figure S1 the current-voltage characteristic of the various optoelectronic components considered for dual radiative engines [1]. Two of them produce electrical power (TR and PV cells) while the two others consume power (LEDs and NEL diodes).

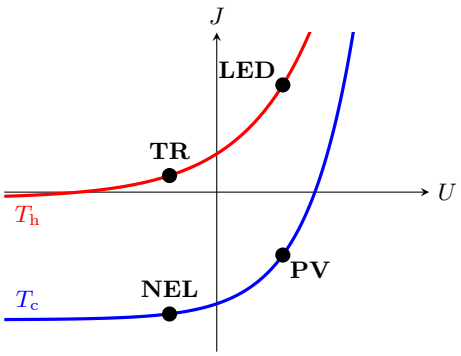

FIG. S1: Schematic of current-voltage characteristics of optoelectronic devices. $U \cdot J > 0$ means that electrical power is consumed.

II. PERFORMANCE OF DUAL ENGINES FOR LOW BANDGAPS

We provide in Fig. S2 the variation of electrical power output and cooling power as a function of both chemical potentials, this time for $E_g = k_B T_h$. In comparison to the results obtained for larger bandgaps, the gap between the heat engine and heat pump operating regions is larger. The change is particularly visible in the TPX quadrant, since then $E_g - \mu_i$ becomes lower than $k_B T_i$. In this quadrant, the device is almost always capable of operating as a heat engine as long as $\mu_c \geq \mu_h$. Consequently, TPX devices are not able to operate as heat pumps for such low bandgaps.

III. IMPACT OF NON-RADIATIVE LOSSES ON $\eta - P$ CHARACTERISTICS

The results presented in the main article are obtained at the radiative limit, and therefore provide an upper bound for dual radiative engines' performance. Obviously, if non-radiative losses are included, performance will be worsened: we aim at giving here some first insights about the impact of such losses. To do so, we manually set the quantum efficiency (QE), defined as the fraction of recombinations being radiative, to 0.9 for both components of the dual engine. This means that 10% of the total recombination rate can be attributed to non-radiative losses. Since the non-radiative generation rate must balance the non-radiative generation rate at equilibrium, we get a new expression of the power generated

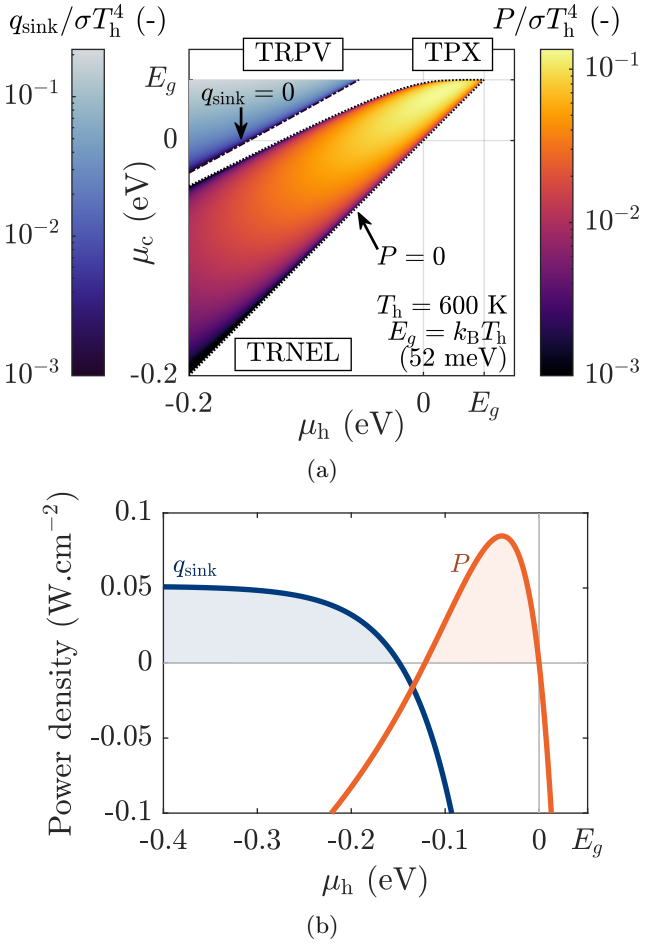

FIG. S2: (a) Performance of dual radiative systems operating as heat engines or heat pumps, at the radiative limit and for $E_g = k_B T_h = 52$ meV. (b) Zoom on the $\mu_c = 0$ scenario.

by an optoelectronic component [2]:

$$P_i = \mu_i \left(\dot{N}_j - \dot{N}_i - \frac{1-\mathrm{QE}}{\mathrm{QE}} \left(\dot{N}_i - \dot{N}_i(\mu_i = 0) \right) \right). \quad (1)$$

For a 600 K heat source temperature, the use of this expression leads to the $\eta - P$ plots illustrated in Fig. S3. Several major differences appear in comparison to the results obtained at the radiative limit. First, TRNEL devices have significantly lost interest, since they are no longer able to reach Carnot efficiency. Worse, their envelope is now within that of TRPV devices for both bandgaps considered. Therefore, TRNEL systems have interest only when operating close enough to the radiative limit. Second, the maximum efficiency is now highly dependent on the bandgap: being only 40% of Carnot efficiency for $E_g = k_\mathrm{B}T_\mathrm{h}$, it goes up to 80% of η_C for $E_g = 10k_\mathrm{B}T_\mathrm{h}$. Last, the power output variation with the bandgap is way weaker; in fact, as long as QE < 1, there is an optimal bandgap that allows maximising the power output [3] (page 61).

Additionally, including non-radiative losses causes a mismatch between the currents J_h and J_c of the two optoelectronic components. Since voltages are mismatched too, the two components cannot be directly bound electrically if both have the same area, and additional electronics is necessary to make the engine work. Otherwise, it is possible to design engines with components with mismatched areas [4] or bandgaps [5] to make them self-sustaining.

IV. IMPACT OF HEAT SOURCE TEMPERATURE ON $\eta - P$ CHARACTERISTICS

In Fig. S4 and S5 are provided $\eta - P$ plots obtained at the radiative limit, but respectively for a 400 K and 1200 K heat source temperature. The conclusion drawn for $T_\mathrm{h} = 600$ K remains valid in these scenarios. We can still notice two slight differences. First, the normalised power output achieved becomes larger as T_h increases. Considering $E_g = 10k_\mathrm{B}T_\mathrm{h}$ for instance, $P_\mathrm{max}/\sigma T_\mathrm{h}^4$ equals approximately 0.6 for $T_\mathrm{h} = 400$ K, but goes up to 2.4 for $T_\mathrm{h} = 600$ K and exceeds 5 for $T_\mathrm{h} = 1200$ K. Second, the interest of TRPV devices rises with temperature, more and more of the total envelope corresponding to that of the TRPV device if the bandgap stays moderate. For $T_\mathrm{h} = 1200$ K and $E_g = k_\mathrm{B}T_\mathrm{h} \approx 0.1$ eV, TRPV gives access to interesting trade-offs between power and efficiency. However, note that such high temperatures can hardly be withstood by optoelectronic components, and therefore limits TRPV interest.

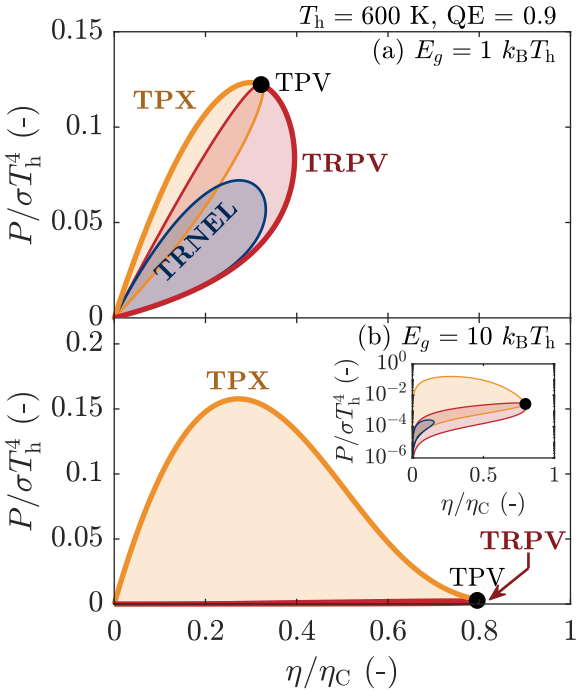

FIG. S3: $\eta - P$ plots obtained for dual radiative engines, for $T_\mathrm{h} = 600$ K and for various bandgaps. A quantum efficiency of 0.9 is considered.

V. VARIATION OF MAXIMUM POWER AND RELATED EFFICIENCY WITH BANDGAP

We provide in Fig. S6 the variations of the maximum power and related efficiency as a function of the bandgap, respectively for the complete dual engine (thick black line) and for each individual engine. For a heat source temperature of 600 K, the dual engine MPP moves from the TRPV quadrant for low bandgaps to the TPX quadrant for higher bandgaps. In this case, the transition between the two quadrants occurs around $E_g/k_\mathrm{B}T_\mathrm{h} = 0.7$. Dual engines become especially attractive when $E_g > k_\mathrm{B}T_\mathrm{h} \approx 0.05$ eV, their power output increasing with E_g and being already 50% larger than that of single engines for $E_g = 1.9k_\mathrm{B}T_\mathrm{h}$. In practice, this condition is satisfied by any realistic bandgap at the temperature considered.

Note how, when TPX or TRPV engines do not maximise the power output, they operate as TPV devices. This is what causes the sudden change in slope observable in panel (b): around $E_g/k_\mathrm{B}T_\mathrm{h} = 0.7$, there is for both devices an abrupt change in the direction of displacement of the MPP in $(\mu_\mathrm{h}, \mu_\mathrm{c})$ coordinates, from that of the complete dual engine to that of a TPV device (or vice-versa).

One can also observe that optimising TRNEL devices for electrical power production simply means operating as a TR device. Moreover, in the limit of zero bandgap, TR operation becomes optimal: this is because the TRNEL quadrant is the only one available since $\mu < E_g \to 0$.

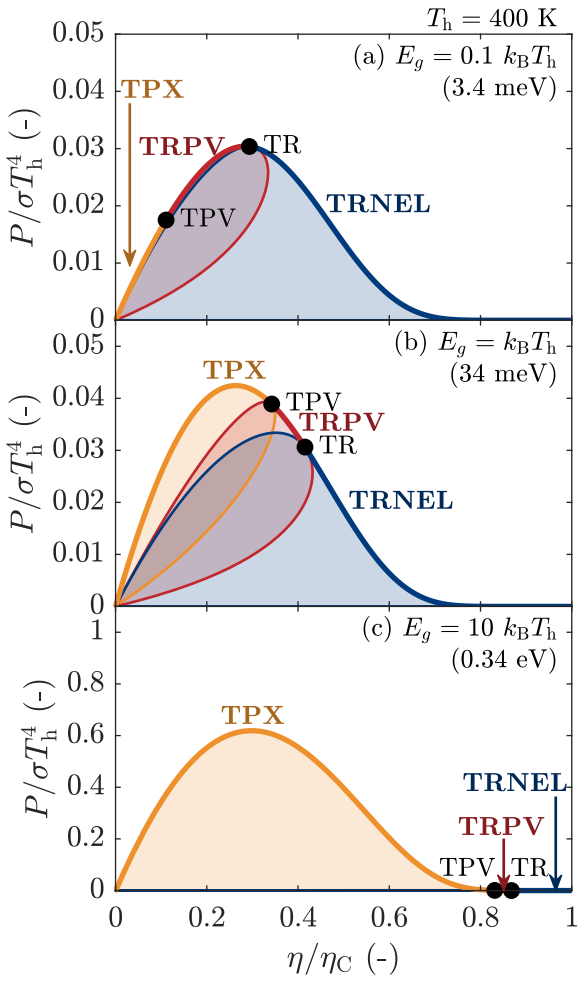

FIG. S4: $\eta - P$ plots obtained for dual radiative engines at the radiative limit, for $T_h = 400$ K and for various bandgaps.

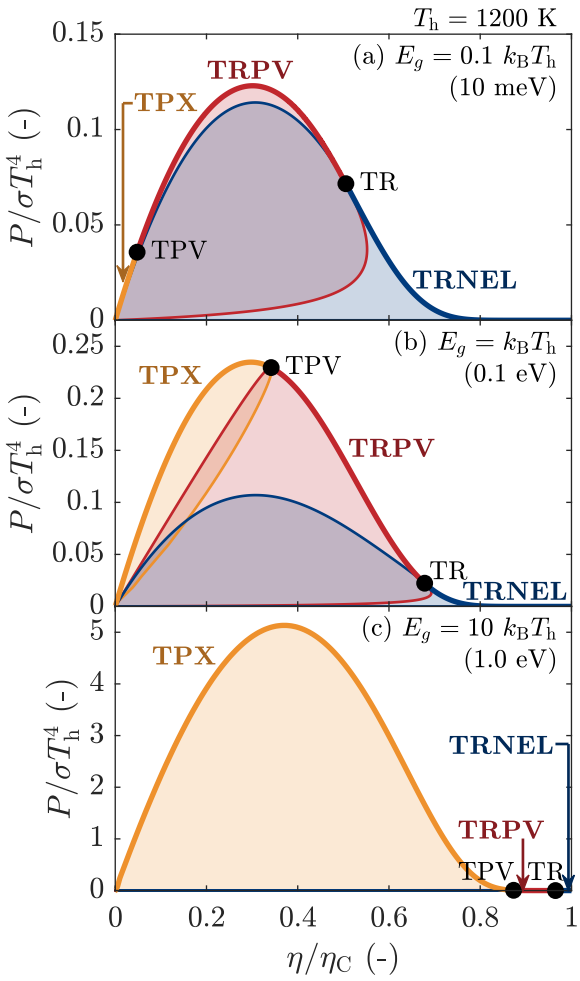

FIG. S5: $\eta - P$ plots obtained for dual radiative engines at the radiative limit, for $T_h = 1200$ K and for various bandgaps.

VI. DETERMINATION OF THE CHEMICAL POTENTIALS AT MAXIMUM POWER

The goal is to determine the couple (X_h, X_c) which allows maximising P:

$$P = \frac{E_g^2 k_B^2 T_h^2}{4\pi^2 c^2 \hbar^3} \left(\ln(X_h) - \frac{T_c}{T_h} \ln(X_c) \right) \times \left(\ln(1 - X_h) - \frac{T_c}{T_h} \ln(1 - X_c) \right). \tag{2}$$

The first thing to verify is whether the maximum power is reached inside the domain (i.e. for $0 < X_i < 1$) or at the boundary. For instance, if X_h goes to 0, it gives

$$P \sim -\frac{E_g^2 k_B^2 T_h^2}{4\pi^2 c^2 \hbar^3} \ln(X_h) \ln(1 - X_c) \frac{T_c}{T_h} \to -\infty, \tag{3}$$

and the maximum power is therefore not reached at this boundary (the power being negative). A similar treatment can be done at the three other boundaries to ensure that the maximum power point is indeed located inside the domain. We should then find the couple (X_h, X_c) which makes both partial derivatives equal to zero. If the couple found is unique, it is the maximum power point since P goes to $-\infty$ at the boundaries (which means that a maximum power point must exist).

Setting both partial derivatives of P with respect to X_i to zero, we get

$$\frac{\ln(1 - X_h) - \ln(1 - X_c)\frac{T_c}{T_h}}{\ln(X_h) - \ln(X_c)\frac{T_c}{T_h}} = \frac{X_h}{1 - X_h}, \tag{4a}$$

$$= \frac{X_c}{1 - X_c}. \tag{4b}$$

Note that this holds only if $\ln(X_h) - \ln(X_c)\frac{T_c}{T_h}$ is non-zero at the maximum power point. If the former term was equal to zero, then $\ln(1 - X_h) - \ln(1 - X_c)\frac{T_c}{T_h}$ should also be zero to satisfy that partial derivatives are equal to zero, which would lead to $1 - X_c^{T_c/T_h} = (1 - X_c)^{T_c/T_h}$. This equation being satisfied only for X_c equal to 0 or 1

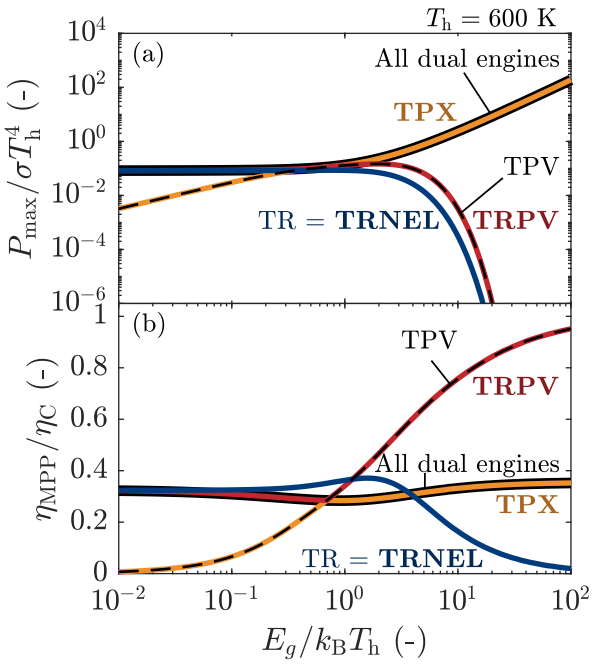

FIG. S6: Variation of (a) the maximum power, (b) the efficiency at maximum power, for the different radiative engines considering $T_h = 600$ K.

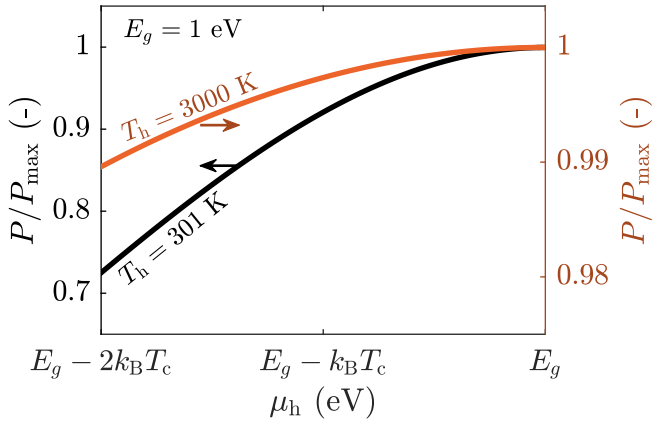

FIG. S7: Variation of the power output with the LED chemical potential considering quasi-monochromatic radiation exchanged, for $E_g = 1$ eV and for two heat source temperatures. In this case, only the TPX quadrant is considered.

(which are not inside the domain), $\ln(X_h) - \ln(X_c)\frac{T_c}{T_h}$ is therefore non-zero at the maximum power point.

Combining the two expressions given in Eq. (4), we easily get that $X_h = X_c$. Writing this common value X, we obtain

$$P = \frac{1}{\hbar}\left(\frac{E_g k_B (T_h - T_c)}{2\pi c\hbar}\right)^2 \ln(X)\ln(1-X). \quad (5)$$

Notice how P is symmetric around the axis $X = 1/2$ (since $P(X) = P(1-X)$): at $(X_h = 1/2, X_c = 1/2)$, both partial derivatives therefore equal zero. In fact, this couple is the only possible solution, and corresponds thus to the maximum power point.

VII. IMPACT OF THE CHEMICAL POTENTIAL OF QUASI-MONOCHROMATIC RADIATION

In the article, to derive an expression of the efficiency at maximum power in the case of quasi-monochromatic radiation exchanged, we state that $E_g - \mu_i \ll k_B T_i$. To verify this, we show in Fig. S7 the variation of power output with μ_h for $E_g = 1$ eV, considering only the TPX quadrant. The power output associated to each μ_h corresponds to the maximum achievable with the whole range of μ_c available. We observe that $E_g - \mu_{h,MPP} \ll k_B T_c$: since $T_h > T_c$, therefore $E_g - \mu_{h,MPP} \ll k_B T_h$. Moreover, $\mu_c \geq \mu_h$, and thus $E_g - \mu_{c,MPP} \ll k_B T_c$.

VIII. MODIFICATION OF THE ACHIEVABLE OPERATING CONDITIONS UNDER SPECTRAL FILTERING

To study the impact of spectral filtering (i.e. of reducing the radiation bandwidth δE), we show in Fig. S8 how the $\eta - P$ envelope of dual engines vary with δE. In addition, the complete set of operating conditions achievable by varying δE is represented by the grey area. Three different scenarios are considered to highlight the variability of the influence of spectral filtering on the achievable operating conditions.

The envelopes obtained at the radiative limit for a bandgap of $k_B T_h$ are shown in panel (a), the results being mostly similar to those obtained at $E_g = 10 k_B T_h$. In this scenario, filtering gives access to new operating conditions in the high-efficiency region. For $P/\sigma T_h^4 < 0.03$, this can allow increasing the efficiency by up to 10 percent points. The effect is even stronger when decreasing the quantum efficiency (QE) to 0.9 (see Section III for more details on QE), as depicted in panel (b): an efficiency increase of the order of 25 percent points can be reached for $P/\sigma T_h^4 = 0.03$, and goes up to 45 percent points for $P/\sigma T_h^4 = 0.01$. In this case, the MPP obtained with filtered radiation can even move beyond the envelope obtained in the broadband scenario. In other words, spectral filtering can limit the power loss undergone in high-efficiency operation.

There are however cases where filtering has no significant benefit. We provide one such example in panel (c), obtained for QE $= 0.9$ and $E_g = 10 k_B T_h$. Under such conditions, reducing the bandwidth mostly make the envelope shrink, the only benefit being a small increase of the efficiency achieved for powers close to zero. In such scenarios, it is thus better to prevent filtering radiation.

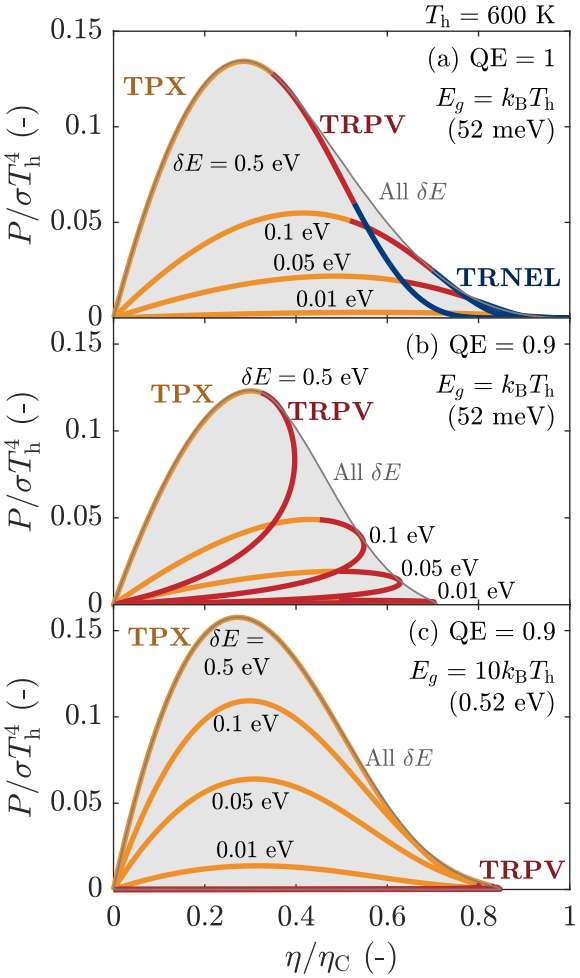

FIG. S8: Dual radiative engine $\eta - P$ envelopes obtained for varying spectral bandwidth δE.

[1] E. J. Tervo, E. Bagherisereshki, and Z. M. Zhang, Near-field radiative thermoelectric energy converters: a review, Frontiers in Energy **12**, 5 (2018).

[2] J. Legendre and P.-O. Chapuis, GaAs-based near-field thermophotonic devices: Approaching the idealized case with one-dimensional PN junctions, Solar Energy Materials and Solar Cells **238**, 111594 (2022).

[3] J. Legendre, *Theoretical and numerical analysis of near-field thermophotonic energy harvesters*, Ph.D. thesis, INSA Lyon, available at `https://theses.fr/2023ISAL0094` (2023).

[4] B. Zhao, S. Buddhiraju, P. Santhanam, K. Chen, and S. Fan, Self-sustaining thermophotonic circuits, Proceedings of the National Academy of Sciences **116**, 11596 (2019).

[5] Z. Yang, J. Song, and B. J. Lee, Thermophotonic cells in self-sustaining parallel circuits, Journal of Quantitative Spectroscopy and Radiative Transfer **312**, 108792 (2024).